Systematics of zircaloy-4 lattice parameters from 2 K to PWR irradiation conditions

G. Noguere, S. Xu, A. Filhol, J. Ollivier, J.-M. Zanotti, Quentin Berrod, V. Nassif, I. Puente Orench, Claire Colin, T C Hansen, et al.

Systematics of zircaloy-4 lattice parameters from 2 K to PWR irradiation conditions

G. Noguere[1,a], S. Xu[1], A. Filhol[2], J. Ollivier[2], J.-M. Zanotti[3], Q. Berrod[4], V. Nassif[5], I. Puente Orench[6], C. Colin[5], T. C. Hansen[2], D. Bernard[1]

[1] CEA, DES, IRESNE, DER, Cadarache, 13108 Saint Paul Les Durance, France

[2] Institut Laue-Langevin, 38042 Grenoble, France

[3] Laboratoire Leon Brillouin (CEA-CNRS), Universite Paris-Saclay, CEA Saclay, 91191 Gif-sur-Yvette Cdex, France

[4] CNRS-CEA-Universite Grenoble Alpes, SyMMES, 38000 Grenoble, France

[5] Universite Grenoble Alpes, Institut Néel, 38000 Grenoble, France

[6] Instituto de Nanociencia y Materiales de Aragòn, CSIC, Pedro Cerbuna 12, 50009 Zaragoza, Spain

Received: 26 June 2024 / Accepted: 19 August 2024

Abstract Below a few eV, interactions of neutrons with zircaloy-4 depend on the structure of the material and of the dynamics of each atom in the crystal, which are described by the lattice parameters and the phonon density of states, respectively. Despite the numerous works performed on zircaloy-4, the systematic variation of the lattice parameters up to normal pressurized water reactor (PWR) operating conditions was never explicitly reported in the literature. Similarly, it was not possible to find studies reporting any theoretical of experimental phonon density of states for zircaloy-4. The goal of this study is to provide the variation of the lattice parameters of α-Zr in zircaloy-4 as a function of nuclear fuel burnup in the temperature range over which the hexagonal phase exists. For that purpose, lattice parameters for low-hydrogenated Zy4 samples have been determined thanks to new diffraction experiments performed with the D1B instrument of the Institut Laue-Langevin (ILL, Grenoble, France) from 2 to 300 K. Past neutron diffraction experiments carried out with the D20 instrument were used to provide consistent lattice parameters from 300 to 700 K. Then, irradiation growth of zircaloy-4 under neutron irradiation was added as correction factors by using results reported in the literature. Parallel inelastic neutron scattering experiments were also performed on the IN5 and IN6 time-of-flight spectrometers in order to measure the phonon density of states of zircaloy-4 at room temperature for its subsequent use in the calculation of the Debye–Waller coefficient and Debye temperature which are involved in the determination of the lattice parameters.

1 Introduction

Interest in zirconium alloys as nuclear fuel rod cladding arose in the early days of the nuclear industry [1]. Zircaloy refers to a group of alloys that can be differentiated by the percentage of metals added to zirconium (Zr) with the aim of increasing the resistance to high-temperature water corrosion and the mechanical strength of cladding. In pressurized water reactor (PWR), the main addition to zircaloys-4 (Zy4) is tin (Sn, □ 1.5%) together with a small amount of iron (Fe, □ 0.2%) and chromium (Cr, □ 0.1%). Numerous studies on the high-temperature oxidation mechanisms of zircaloy in water have highlighted the major role of the intermetallic precipitates $Zr(Fe,Cr)_2$ and zirconium hydride (ZrH_x) in the production rate of zirconia layer (ZrO_2) [2–5]. Other Zr-based nuclear fuel claddings were subsequently developed, such as ZIRLO^{TM} and M5^{TM} which contains niobium, to improve corrosion resistance and limit the absorption of hydrogen which chemically bonds with zirconium.

In this work, we are mainly interesting by the physical parameters involved in the calculation of the low-energy neutron scattering cross section on zircaloy-4 as a function of temperature and neutron irradiation conditions. Below a few eV, interactions of neutrons with zircaloy-4 depend on the structure of the material and of the dynamics of each atom in the crystal, which are described by the lattice parameters and the phonon density of states, respectively. The lattice parameters increase with the temperature because of thermal expansion. However, under neutron irradiation, growth strain mechanisms dominate the lattice parameter changes. In this context, our work specifically focused on the influence of the hydrogenation process and of the dislocation loops that form in zircaloy-4 under neutron irradiation. The aim of the study is to propose a systematic variation of the lattice parameters of zircaloy-4 from 2 K to normal PWR operating conditions, which correspond to temperatures lower than 700 K.

Compared to the well-documented neutron scattering studies of pure α-Zr, those for α-Zr in zircaloy-4 are scarce in the literature. The first step of this work consisted in determining the variation of the lattice parameters for low-hydrogenated zircaloy-4 samples using an empirical expression relying on the Debye model. For this purpose, diffraction experiments were performed on the D1B instrument of the Institut Laue-Langevin (ILL, Grenoble, France) from 2 to 300 K. For temperatures ranging from 300 to 700 K, we

a e-mail: gilles.noguere@cea.fr (corresponding author)

Published online: 04 September 2024

decided to revisit the data of Lelièvre et al. [6] measured with the D20 instrument of ILL. The second step consisted of taking into account the influence of the irradiation growth as correction terms deduced from results reported in the literature. Parallel inelastic neutron scattering experiments were also performed on the IN5 and IN6 time-of-flight spectrometers in order to measure the phonon density of states of zircaloy-4 at room temperature for its subsequent use in the calculation of the Debye–Waller coefficient and Debye temperature. The originality of this work relies on the Monte Carlo analysis of the neutron scattering data with the Tripoli-4® code [7] in association with the thermal scattering law theory implemented in the CINEL code [8]. Optimized phonon density of states for zircaloy-4 and lattice parameters are natural outcomes of these codes.

The thermal neutron scattering models implemented in the CINEL code are presented in Sect. 2. The neutron scattering experi-ments carried out with the ILL spectrometers are described in Sect. 3. Results for low-hydrogenated samples are reported in Sect. 4. Section 5 presents the variation of the lattice parameters under neutron irradiation.

2 Thermal scattering law theory

Mathematical expressions involved in the thermal scattering law theory are well described in the literature [9–11]. For incident neutron energies lower than a few eV, the neutron scattering cross section in a low-hydrogenated zircaloy sample can be approximated by the sum of a coherent elastic scattering cross section $\sigma_{\mathrm{coh}}^{\mathrm{el}}$, which takes into account the crystalline structure of the material, and an inelastic scattering cross section σ_X^{inel}, which depends on the dynamic properties of each atom X in the crystal. Equations introduced in the CINEL code [8] are described in Sects. 2.1 and 2.2.

2.1 Coherent elastic neutron scattering model

The coherent contribution of the elastic scattering depends on the crystalline structure of the material, which is characterized by a periodic unit cell containing N atoms. In the direct lattice, the unit cell is defined by a set of unit vectors a, b, c of lengths a, b, c and volume $V\, a \cdot (b \times c)$. The angles between them are conventionally denoted by α, β and γ. The position of each atom X located at the point (x_X, y_X, z_X) is given by:

$$p_X \quad x_X a + y_X b + z_X c. \tag{1}$$

In the reciprocal lattice, the unit vectors are defined as:

$$\tau_a \quad \frac{2\pi}{V}(b \times c), \quad \tau_b \quad \frac{2\pi}{V}(c \times a), \quad \tau_c \quad \frac{2\pi}{V}(a \times b), \tag{2}$$

in which Miller indices h, k and l denote reticular planes (hkl) orthogonal to the reciprocal lattice vector:

$$\tau_{hkl} h\tau_a + k\tau_b + l\,\tau_c\,. \tag{3}$$

The coherent elastic scattering emerges from the sum of all neutron scattering contributions over the N atoms of the unit cell and reticular planes (hkl) that are oriented at the correct angle to fulfil the Bragg condition. In this work, this contribution is approximated by the following expression:

$$\sigma_{\mathrm{coh}}^{\mathrm{el}}(E) \quad \frac{\pi^2 \hbar^2}{\mathrm{mNVE}} \sum_{E \geq E_{hkl}} d_{hkl} \left|F(\tau_{hkl})\right|^2 P_{hkl}(\ _{hkl}), \tag{4}$$

in which the crystallographic structure factor is given by:

$$F(\tau_{hkl}) \quad \sum_X^N \frac{b_X}{1_X} \exp\left(-\frac{2\tau_{hkl}^2}{4M_X k_B T}\right)_X e^{i\,\tau_{hkl}\cdot p_X}, \tag{5}$$

where m is the neutron mass, E_{hkl} $\hbar^2\tau_{hkl}^2/(8m)$ represents the Bragg edges, d_{hkl} $2\pi/\tau_{hkl}$ stands for the distance between adjacent reticular planes (hkl), b_X is the coherent bound scattering length and X stands for the Debye–Waller coefficient.

In Eq. (4), $P_{hkl}(\ _{hkl})$ represents a preferred orientation correction which depends on the orientation angle $_{hkl}$ between the preferred orientation vector and τ_{hkl}. This correction can be deduced from experimental diffraction patterns or described by a cylindrically symmetric pole-density distribution function (PDDF). Various types of phenomenological PDDFs are reported in the literature [12]. They will be discussed in Sect. 4.2.

Parameters needed for calculating $\sigma_{\mathrm{coh}}^{\mathrm{el}}$ depend on the structural properties of zircaloy-4. In this section, we restrict ourselves to the atom site occupancy fractions of zirconium, tin, iron, chromium as well as oxygen from oxidation. As zircaloy-4 is made from α-Zr matrix with a small amount of Sn in solid solution, Zr and Sn atoms share the same hexagonal close-packed arrangement (space group P63/mmm). Due to their low solubility, Fe and Cr atoms form intermetallic compounds. They mainly fall into binary Laves phase families of the type Zr(Fe,Cr)2 with a predominant crystallization in hexagonal or face-centred cubic structures, labelled C14 (space group P63/mmm) and C15 (space group Fd-3 m). Under PWR conditions, thin ZrO2 layer that arises during the oxidation

mechanism is a mixture of monoclinic (space group $P2_1/c$) and tetragonal (space group $P4_2/nmc$) zirconia [13]. Tetragonal phase theoretically has no reason to exist under these conditions. However, it could be explained by an optimal size of the ZrO_2 grains, below which the tetragonal ZrO_2 becomes stable [14–16]. Crystallographic information introduced in the calculations has been retrieved from the Material Project database [17].

In this work, lattice parameters for zircaloy-4 have been deduced from diffraction experiments performed with the D1B and D20 instruments from 2 to 700 K using low-hydrogenated samples. The competitive strains between hydrogen and microstructures under neutron irradiation were added as correction terms as a function of nuclear fuel burnup, which were deduced from systematics reported in the literature. Results are discussed in Sect. 4.2 and 5.

2.2 Inelastic neutron scattering model

The double-differential inelastic scattering cross section is related to the dynamic structure factor $S_X(Q, \omega)$ as follows [18, 19]:

$$\frac{d^2\sigma_X^{\text{inel}}(E)}{dE\,d\theta} \quad \frac{\sigma_X}{4\pi} \quad \frac{\overline{E}}{E} S_X(Q, \omega), \tag{6}$$

where E stands for the energy of the neutron scattered at the laboratory angle θ and σ_X is the bound neutron elastic scattering cross section. The dynamic structure factor is defined as a function of the wavenumber transfer Q and energy transfer $\varepsilon\ \omega$. It can be conveniently split in a coherent and incoherent terms:

$$S_X(Q, \omega) S_X^{\text{coh}}(Q, \omega) + S_X^{\text{inc}}(Q, \omega). \tag{7}$$

A suitable analytical expression for the inelastic incoherent term $S_X^{\text{inc}}(Q, \omega)$ is obtained via the so-called phonon expansion method [20, 21]:

$$S_X^{\text{inc}}(Q, \omega) e^{-} \quad \frac{^2 Q^2}{2M_X k_B T} \quad {}_X \sum_{n\ 1}^{\infty} \frac{1}{n!} \quad \frac{^2 Q^2}{2M_X k_B T} \quad {}^n {}_X H_n(\omega), \tag{8}$$

where k_B is the Boltzmann constant, n represents the phonon expansion order, M_X is the mass of the nucleus X, $_X$ stands for the Debye–Waller coefficient and the multiphonon term $H_n(\omega)$ has the generic form:

$$H_n(\omega) \quad \int_{-\infty}^{\infty} H_1(\omega) H_{n-1}(\omega - \omega)\,d\omega. \tag{9}$$

The one-phonon term is given by:

$$H_1(\omega) \quad \frac{1}{{}_X P_X(\omega)}. \tag{10}$$

with

$$_X \quad \int_{-\infty}^{\infty} P_X(\omega)\,d\omega, \tag{11}$$

in which $P_X(\omega)$ is approximated by the following expression:

$$P_X(\omega) \rho_X^{\text{inc}}(\omega) e^{\ ^{2k_B T}} \quad \frac{\omega}{} \quad \frac{2\omega}{k_B T} \sinh \quad \frac{\omega}{2k_B T} \quad {}^{-1}, \tag{12}$$

with

$$\rho_X(\omega) w_c \rho_X^{\text{coh}}(\omega) + w_i \rho_X^{\text{inc}}(\omega). \tag{13}$$

The phonon density of states $\rho_X(\omega)$ is the main physical quantity involved in the theoretical description of the dynamic structure factor. In a first approximation, it can be seen as a combination of the coherent ρ_X^{coh} and incoherent ρ_X^{inc} contributions with the condition $w_c + w_i$ 1. For zircaloy-4, neither theoretical nor experimental $\rho_X(\omega)$ were found in the literature. In this work, $\rho_X(\omega)$ for zircaloy-4 has been deduced from inelastic neutron scattering measurements carried out with the IN5 and IN6 spectrometers of ILL at room temperature. Results are presented in Sect. 4.1.

3 Neutron scattering experiments on low-hydrogenated Zy4 samples

Neutron scattering experiments considered in this work were all carried out at ILL. The neutron diffraction experiments were performed with the D1B and D20 instruments. Those for inelastic neutron scattering were performed with the IN5 and IN6 time-of-flight spectrometers. Data used for D20 were published by Lelièvre et al. [6]. From the point of view of the neutron transport physics, these spectrometers share the same basic design (Fig. 1). The experimental conditions are summarized in Table 1. We will

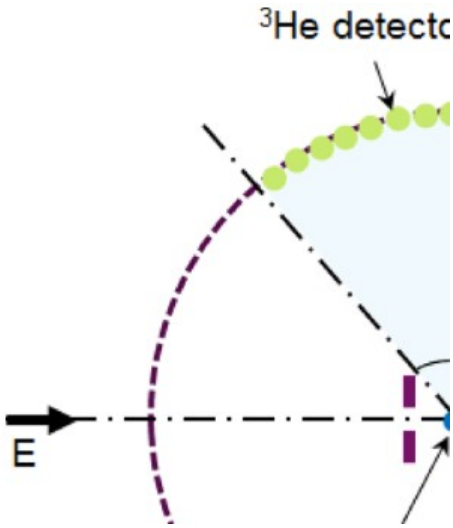

Fig. 1 Simplified top view of the IN5, IN6, D1B, D20 spectrometers. The distance L between the sample and the detector array is equal to 4.00 (1), 2.48 (1), 1.500 (1) and 1.47 (1) m for IN5, IN6, D1B and D20, respectively. Angles θ_{min} and θ_{max} represent the lower and upper limits of the laboratory scattering angle θ

Table 1 Short overview of the experimental conditions. Three low-hydrogenated zircaloy-4 samples were considered in this work. The crosses indicate in which instruments the samples were measured. The composition of each sample is given in Table 2

Spectrometer		IN6	IN5	D20 [6]	D1B
Flight length	(m)	4.00 (1)	2.48 (1)	1.47 (1)	1.500 (1)
Neutron wavelength	(Å)	5.12	4.80	2.42	1.28
Neutron energy	(meV)	3.12	3.55	13.97	49.93
Beam size	(mm^2)	20×50	15×30	20×50	20×50
Temperature	(K)	294	296	294–700	2–300
Zy4 rod sample		×	×		×
Zy4 tube sample		×			
Zy4 ribbon sample				×	

Table 2 Mass fraction (in %) of Zr, Zn, Fe, Cr and O in the zircaloy-4 samples measured at ILL. The rod and tube samples have a similar Zy4 grade and contain a small amount of impurities, such as Hf (61 wppm) and N (30 wppm)

Elements	Zr	Sn	Fe	Cr	O
Zy4 rod sample	98.08	1.47	0.20	0.10	0.15
Zy4 tube sample	98.08	1.47	0.20	0.10	0.15
Zy4 ribbon sample [6]	98.10	1.45	0.22	0.11	0.12

first present the inelastic neutron scattering experiments performed at room temperature from which the phonon density of state of α-Zr in Zy4 will be deduced for its subsequent use in the calculation of the Debye–Waller coefficient X and Debye temperature θ_D.

3.1 Characteristics of the zircaloy-4 samples

Three low-hydrogenated zircaloy-4 samples were considered in this work. The structure and the dynamics of Zy4 have been deduced from a thick rod, a tube and a sample made of thin Zy4 ribbons. The rod sample had a diameter of 1.0 (1) cm and height of 10.0 (1) cm. The tube sample had a similar external diameter of 1.0 (1) cm and height of 10.0 (1) cm with a wall thickness of 0.40 (1) mm. The third sample was filled with ≈100 rectangular Zy4 ribbons (8.5 × 0.2 cm^2) with thicknesses ranging from 100 to 125 μm in approximately 0.3 g of heavy water. The total mass of Zy4 was close to 10 g. The composition of each sample is given in Table 2. The thick rod sample was used for inelastic neutron scattering and diffraction experiments on the IN5, IN6 and D1B instruments. The tube sample was only used for inelastic neutron scattering on IN6. The sample made of Zy4 ribbons was used by Lelièvre et al. [6] for diffraction experiments on D20.

3.2 Inelastic neutron scattering experiments

Inelastic neutron scattering experiments rely on the neutron time-of-flight technique. This technique consists of measuring the time t travelled by the neutrons from their scattering location until their detection at a given laboratory scattering angle θ. If the energies are in eV, the length in m and the time in μs, the non-relativistic time–energy relation $E = (72.298 L/t)^2$ is used to obtain the

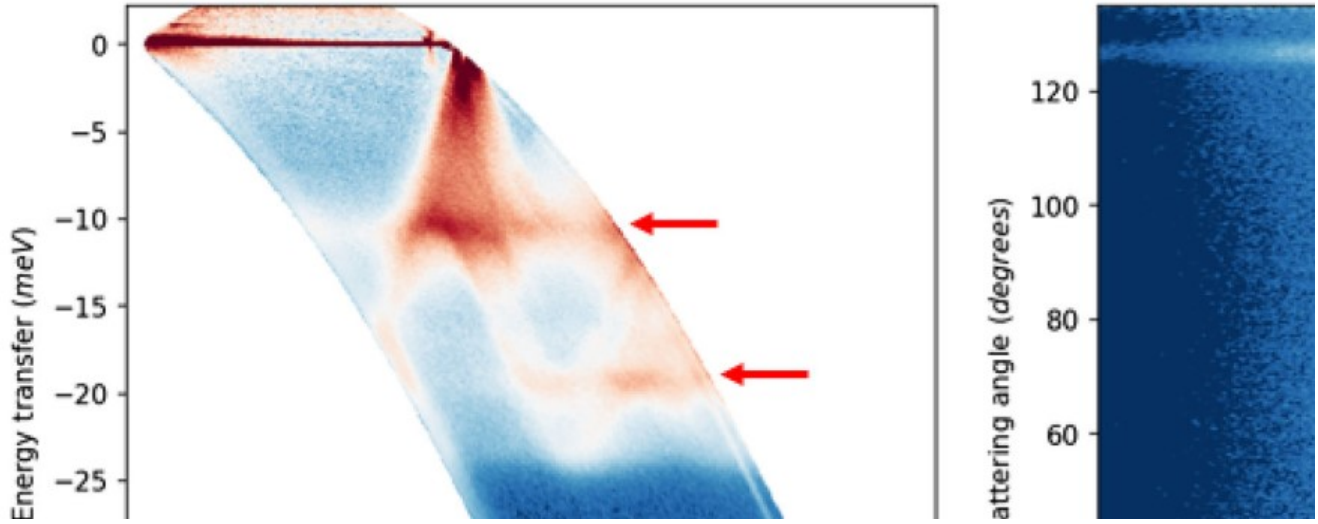

Fig. 2 Dynamic structure factor $S\exp(Q, \omega)$, or equivalently $S\exp(\theta, \omega)$, deduced from IN5 data measured with a Zy4 rod sample at room temperature. The red arrows locate the two main incoherent inelastic contributions

experimental neutron scattering yield $Y_{\exp}^{T}(\theta, E)$ as a function of the outgoing neutron energies E. The distance between the sample and the detection setup is equal to L 4.00 (1) and L 2.48 (1) m, for IN5 and IN6, respectively. Each ^{3}He detector array covers laboratory scattering angles ranging from approximately 10° to 135°. In both cases, a rectangular monoenergetic neutron beam was focused to ziraloy-4 samples with characteristics given in Sect. 3.1. The same Zy4 rod sample was measured with IN6 and IN5 at room temperature. Measurements on IN6 were complemented by a Zy4 tube for investigating the neutron multiple scattering correction.

The experiments consisted in a sequence of sample-in and sample-out measurements, including a short irradiation of a vanadium sample. As this later material nearly behaves as a pure incoherent elastic scatterer, its elastic scattering peak is used as reference for calibration purposes. The data reduction steps were handled with the MANTID [22] and ILL in-house LAMP codes. In both IN5 and IN6 experiments, the background due to neutrons scattered by the sample environment was very low. Figure 2 shows the experimental dynamic structure factor $S_{\exp}$ measured with IN5. It illustrates the coherent and incoherent inelastic coupling dynamics that arises in the crystal lattice of Zy4.

The experimental neutron-weighted multiphonon spectra $\rho_{\exp}(\omega)$ were deduced from the neutron yields $Y_{\exp}^{T}(\theta, E)$ measured on IN5 and IN6 by using the one-phonon expression derived from Eq. (10). For practical applications, the dynamic structure factor can be rewritten in terms of the dimensionless parameters α:

$$\alpha \quad \frac{2\,Q^2}{2M_X k_B T} \quad \frac{E + E - 2\mu\sqrt{E E}}{A_X k_B T}, \tag{14}$$

and β:

$$\beta \quad \frac{\varepsilon}{k_B T} \quad \frac{E - E}{k_B T}, \tag{15}$$

where μ $\cos(\theta)$ is the cosine of the laboratory scattering angle θ, A_X is the ratio of the mass M_X of the scattering atom to the neutron mass and ε ω represents the energy transfer. The relationship between $S_{\exp}(Q, \omega)$ and the symmetric form of the dynamic structure factor $S_{\exp}(\alpha, \beta)$ is given by the following expression:

$$S_{\exp}(\alpha, \beta) \quad \frac{k_B T}{\quad} \; e^{\frac{\omega}{2k_B T}} S_{\exp}(Q, \omega). \tag{16}$$

A compact expression for $\rho_{\exp}(\beta)$ can be obtained by introducing Eq. (10) in Eq. (8). For n 1, we obtain:

$$\rho_{\exp}(\beta) \quad \lim_{\alpha \to 0} \frac{2\beta \sinh \beta/2}{\alpha} S_{\exp}(\alpha, \beta). \tag{17}$$

No attempt was made to iteratively correct the experimental neutron-weighted multiphonon spectra $\rho_{\exp}$ from the multiphonon contribution and the multiple neutron scattering effects. These two effects will be handle through Monte Carlo simulations (Sect. 4.1).

Figure 3 shows the neutron-weighted multiphonon spectra of zircaloy-4 deduced from the IN5 and IN6 data. The good agreement between the rod and tube samples measured with IN6 suggests a low contribution of the multiple neutron scatterings, making

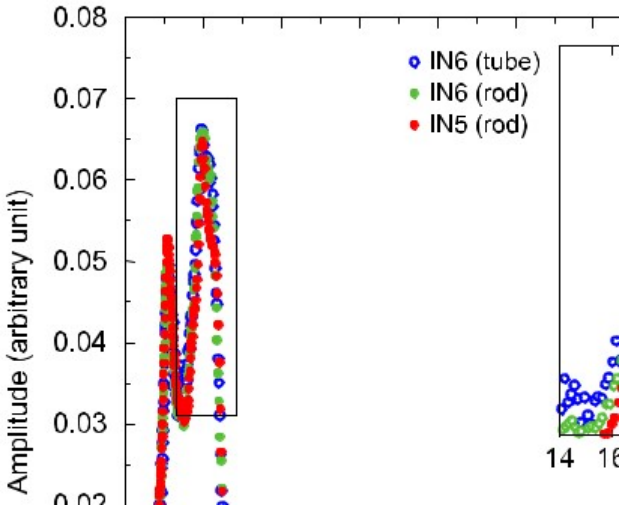

Fig. 3 Experimental neutron-weighted multiphonon spectra $\rho_{exp}(\varepsilon)$ (Eq. (17)) of zircaloy-4 measured with the IN5 and IN6 spectrometers at room temperature. The data are normalized to the 1st peak at 11 meV. The arrow indicates a structure at 53 meV not predicted in the case of α-Zr. The broad structure around 150 meV corresponds to the high frequency vibrations of hydrogen atoms in zirconium hydride (ZrH_x)

this correction rather negligible for the rod sample. Due to its longer flight path and the defocalization effect on IN6, the IN5 instrument has a higher time resolution than IN6, allowing a better description of the acoustic phonon modes of Zy4 around 20 meV. The shoulders on either side of the peak at 20 meV correspond to fines structures which are smoothed out by the time resolution broadening. The weak broad structure around 150 meV also confirms the low hydrogen content in the Zy4 samples. It corresponds to the high frequency vibrations of hydrogen atoms in zirconium hydride (ZrH_x). A surprising small structure, not predicted in the case of α-Zr, can be observed at around 53 meV in both rod and tube samples. The corresponding frequency of about 13 THz (or □ 430 cm^{-1}) is too high for intermetallic precipitates [23], and its shape seems to be too sharp compared to theoretical and experimental phonon densities of states of ZrO_2 [24, 25]. Candidate phonon modes to explain this structure could be attributed to zirconium nitride compounds [26]. Optical mode frequencies calculated for ZrN range between 450 and 500 cm^{-1} [27], which corresponds to an energy transfer slightly higher than that observed, lying between 55 and 62 meV. Complementary theoretical calculations would be valuable to verify whether other $Zr_x N_y$ compounds could be at the origin of this structure coming from a long nitriding process under room temperature conditions.

3.3 Neutron diffraction experiments

Two experiments based on the neutron diffraction technique were investigated to study the structure of Zy4 up to normal PWR operating conditions. We used older diffraction patterns measured with D20 to study the temperature range from 300 to 700 K [6]. The low temperature range (from 2 to 300 K) was covered with new measurements carried out with D1B. A short overview of the experimental conditions is reported in Table 1. The experimental technique for D1B and D20 consists in measuring the neutron scattering yield $Y_{exp}^{T}(\theta)$ as a function of the laboratory scattering angle θ and temperature T . The angle θ $2\theta_{hkl}$ is equivalent to two times the angle θ_{hkl} between the incident neutron beam and the crystallographic reflecting plane. The two instruments nearly share the same geometry. The difference between the incident neutron energies of 49.93 meV (for D1B) and 13.97 meV (for D20) results in a greater contribution from inelastic neutron scatterings in the case of D1B, inducing a smooth background between the Bragg peaks which increases slightly with the laboratory scattering angle.

For D1B, measurements were performed with the same rod sample as used for IN5 and IN6 (Sect. 3.2). The experiment consisted of one-hour measurements for each temperature. A broad temperature step of 40 K was used from 2 to 300 K for determining the smooth increase of the lattice parameters with the temperature. Figure 4a shows the 9 diffraction patterns obtained with D1B. The grey zone highlights the contribution of the intermetallic precipitates at around a laboratory scattering angle of 35°.

For D20, Zy4 ribbons in heavy water (D_2O) was heated at 700 K during 48 h. Diffraction patterns were recorded every 300 s in order to follow the oxidation mechanisms as a function of time. Figure 4b and c reports examples of patterns measured during the heating and cooling periods. Before heating, the broad inelastic scattering contribution of heavy water is well observed at room temperature. Its contribution is surprisingly smoothed out above 400 K with the temperature increase. This rapid change in the contribution of D_2O is difficult to explain. After heating, the main peaks of ZrO_2, around 45° and 85°, reach intensities similar to the intermetallic precipitates, observed at around 70°. Their intensities as a function of time are discussed by Lelièvre et al. in Ref. [6]. They noted a rapid and smooth increase of a zirconia layer (~1.5 μm) composed of monoclinic (□ 75%) and tetragonal (□ 25%) ZrO_2. Figure 5 compares Bragg peaks of α-Zr at around θ 57° before and after heating the sample at 700 K for 48 h. After heating, the position of each peak remains rather unchanged indicating a negligible effect of the deuteration of zircaloy on the lattice parameters. However, we can observe an increase of the peak intensities with the temperature decrease and a reduction of their full width at half maximum by at least 5% at 400 K, certainly due to a texture effect enhanced by the long heating and rapid cooling phases. This effect will be taken into account in the data analysis by using a preferred orientation correction (see Eq. (4)).

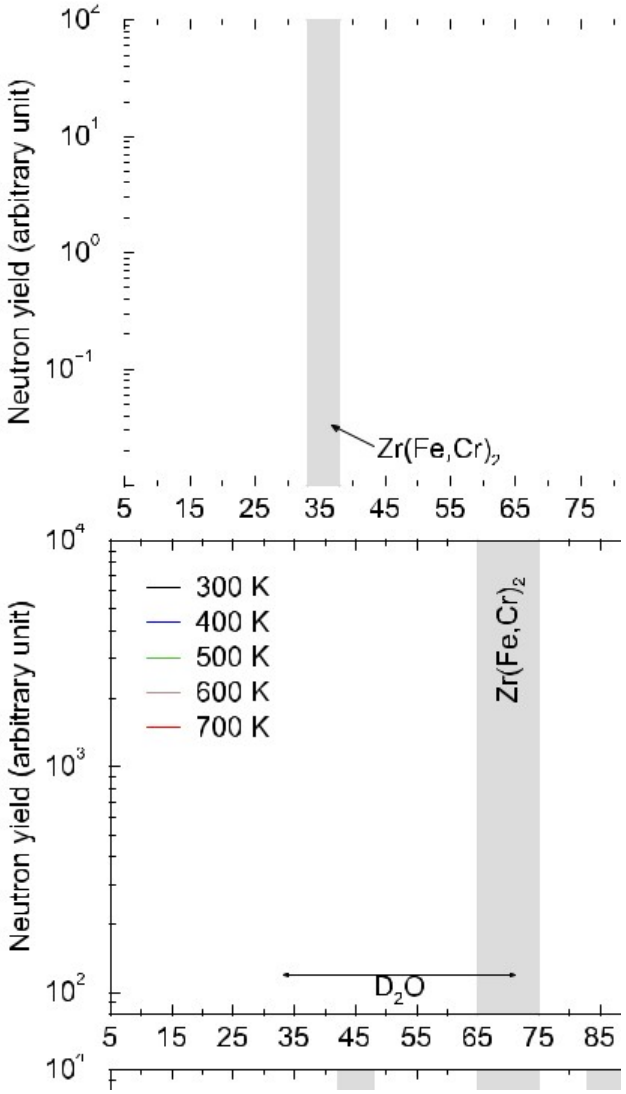

Fig. 4 Diffraction patterns of zircaloy-4 measured with D1B (1.28 Å) and D20 (2.42 Å) [6]. The laboratory scattering angle θ is equivalent to two times the angle θ_{hkl} between the incident neutron beam and the crystallographic reflecting plane. The top plot **a** shows results obtained with D1B at 2, 40, 80, 120, 160, 200, 240, 280 and 300 K. The middle plot **b** reports examples of patterns measured with D20 from 300 to 700 K. The bottom plot **b** shows those obtained during cooling after 48 h at 700 K

4 Results for low-hydrogenated samples

Diffraction and inelastic neutron scattering data measured with the IN5, IN6, D1B and D20 instruments have been analysed using Monte Carlo neutron transport simulations. A two-step calculation scheme was used. The first step consists in producing with the CINEL code [8] a library that contains temperature-dependent neutron scattering cross sections (Sect. 2). The second step consists in calculating the theoretical neutron scattering yield Y_{th}^{T} with the Monte Carlo neutron transport code Tripoli- 4®[7]. Such a data analysis allows taking into account both multiple neutron scattering effects and multiphonon contributions. Principles of the calculations are described in Refs. [28–30]. The inelastic neutron scattering experiments were used to extract the phonon density of states of Zy4 at room temperature. The diffraction experiments were used to determine the lattice parameters from 2 to 700 K.

4.1 Phonon density of states

The phonon density of states of Zy4 were extracted from the experimental neutron scattering yield $Y_{\text{exp}}^{T}(\theta, E)$ (or equivalently from the experimental symmetric dynamic structure factor) measured with IN5 and IN6. For that purpose the time of flight t of each neutron has been simulated without taking into account the time distribution of the initial neutron burst impinging the sample. Therefore, the theoretical neutron scattering yield $Y_{\text{th}}^{T}(\theta, E)$ is calculated from the time-dependent neutron yield $Y_T{}^{T}4(\theta, t)$ provided by Tripoli- 4® as follows:

$$Y_{\text{th}}^{T}(\theta, E) \quad \int_{0}^{+\infty} R_E(\theta, t) Y_T{}^{T}4(\theta, t)\,\mathrm{d}t\,. \tag{18}$$

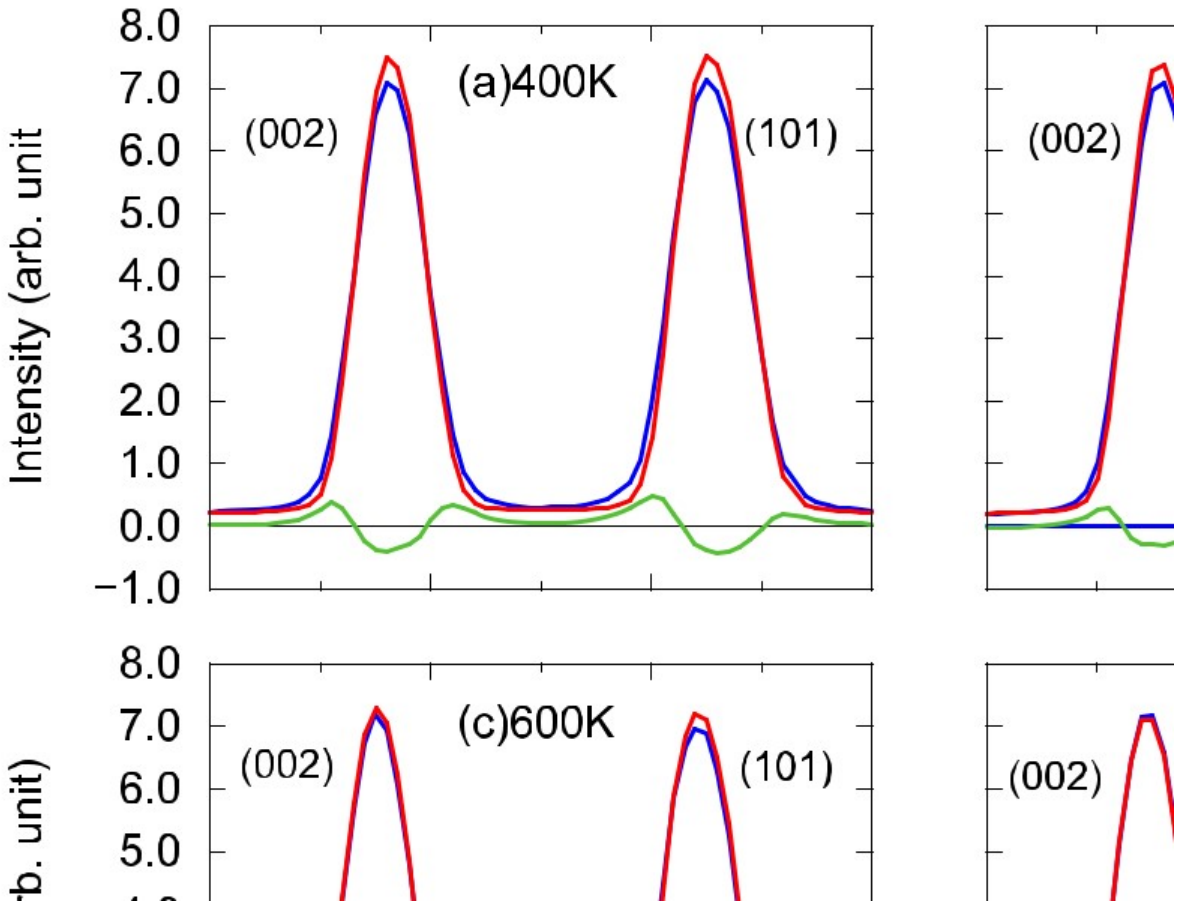

Fig. 5 Comparison of two α-Zr Bragg peaks measured with D20 before (solid blue line) and after (dashed red line) heating the Zy4 sample at 700 K during 48 h. The solid green lines represent the differences between the two curves

The probability density function $R_E(\theta, t)$ stands for the time-dependent experimental response function of the spectrometer which is well approximated by a pseudo-Voigt distribution. Its full width at half maximum was fitted to the neutron elastic scattering peak of vanadium. The theoretical neutron-weighted multiphonon spectra ρ_{th} is subsequently deduced from $Y_{\text{th}}^{T}(\theta, E)$ under the one-phonon approximation (Eq. (17)).

Figure 6 compares the experimental and theoretical symmetric dynamic structure factors obtained after optimization of the incoherent contribution $\rho_X^{\text{inc}}(\omega)$ involved in Eq. (12). In this case, the Tripoli- 4® simulations contain the inelastic incoherent term only. This comparison confirms that the inelastic incoherent contribution alone cannot reproduces the experimental results. Therefore, the (Q, ω)-dependence of the coherent part S_X^{coh} was then reproduced with pseudo-Voigt distributions. Final Tripoli-4® simulations are reported in Fig. 7 for forward and backward laboratory scattering angles. A qualitative agreement with the data is achieved. Model approximations can explain some of the observed differences such as a possible underestimation of the multiphonon contribution at forward angles and an overestimation of the intensity of the first acoustic mode at backward angles due to missing interference terms. Despite these issues, final Tripoli- 4® simulations are able to correctly reproduce the experimental neutron-weighted multiphonon spectra of zircaloy-4, as shown in Fig. 8.

The phonon density of states $\rho_X(\omega)$ of α-Zr in Zy4 obtained in this work from the IN5 and IN6 data, and used in the Tripoli-4® simulations, is shown in Fig. 9a. Values as a function of the energy transfer are reported in Table 3. Maxima of the PDOS are well observed at around 11 and 20 meV. Fine structures of small amplitude were added to slightly improve the description of the shoulder observed in the data around 20 meV. It is satisfying to obtained peak positions that agree pretty well with theoretical predictions reported in Fig. 9b for pure α-Zr. This result confirm that Zr atom vibrations dominate the dynamic properties of Zy4.

4.2 Lattice parameters

The diffraction patterns measured with D1B and D20 were analysed by applying a Rietveld-type structure refinement [33] on the neutron scattering yields simulated with the Tripoli- 4® code. Such an approach makes it possible to correctly account for the transport of neutrons in the sample until their detection as well as background due to inelastic neutron scattering.

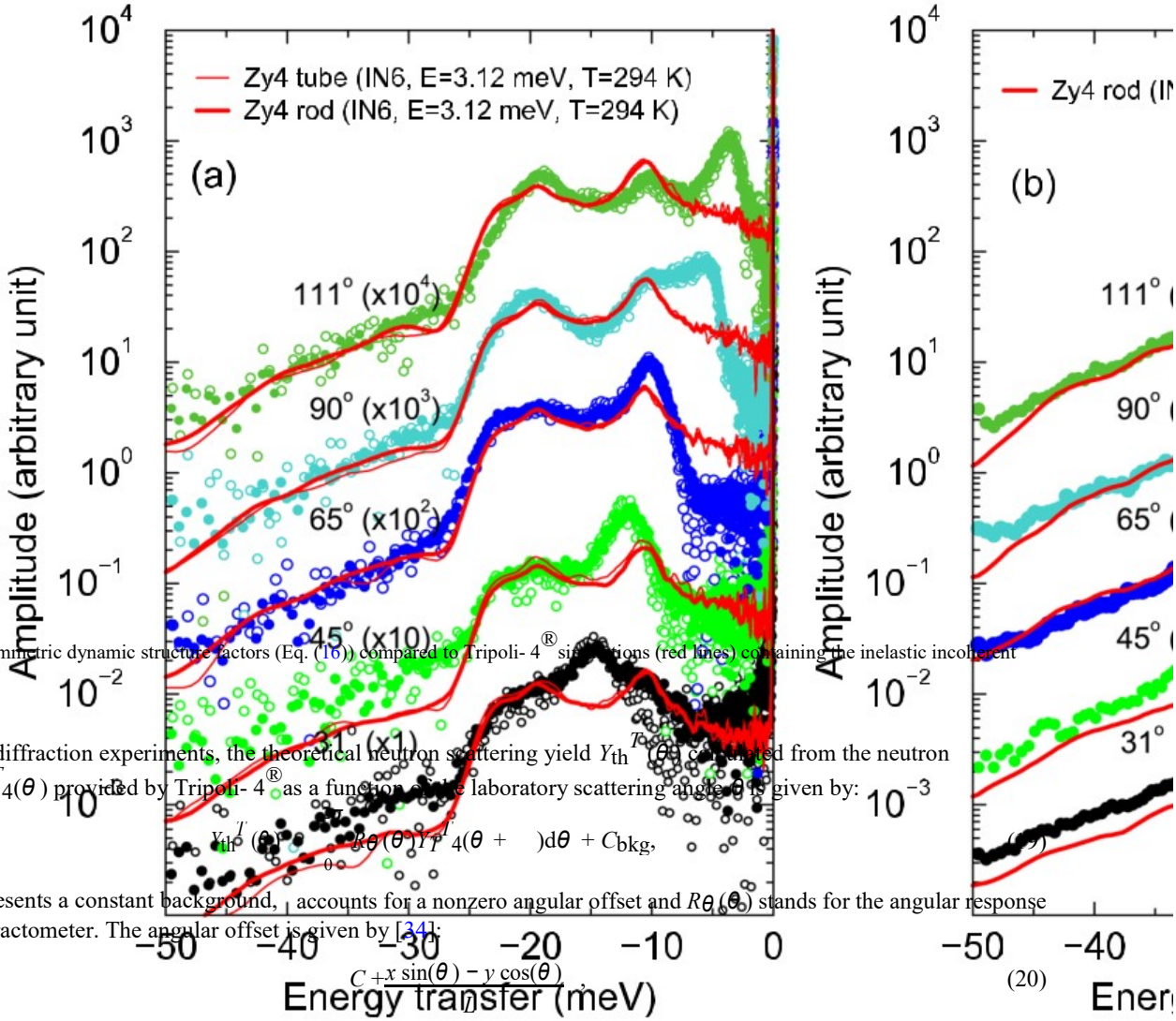

Fig. 6 Experimental symmetric dynamic structure factors (Eq. (16)) compared to Tripoli- 4® simulations (red lines) containing the inelastic incoherent term only

For the neutron diffraction experiments, the theoretical neutron scattering yield $Y_{\mathrm{th}}^{T}(\theta)$ is calculated from the neutron scattering yield $Y_T{}^{T}{}_4(\theta)$ provided by Tripoli- 4® as a function of the laboratory scattering angle θ is given by:

$$Y_{\mathrm{th}}^{T}(\theta) = \int_0^{\pi} R_\theta(\theta')\, Y_T{}^{T}{}_4(\theta + \quad)\mathrm{d}\theta + C_{\mathrm{bkg}}, \tag{19}$$

in which C_{bkg} represents a constant background, accounts for a nonzero angular offset and $R_\theta(\theta)$ stands for the angular response function of the diffractometer. The angular offset is given by [34]:

$$C + \frac{x\sin(\theta) - y\cos(\theta)}{L}, \tag{20}$$

where C is a constant angular shift and (x, y) accounts for the sample displacement from the centre of the diffractometer of radius L. In this work, the angular response function $R\theta$ is approximated by a pseudo-Voigt function with a full width at half maximum R given by the Caglioti expression [35]:

$$_R(\theta) \quad U_1 \tan^2\frac{\theta}{2} + U_2 \tan\frac{\theta}{2} + U_3, \tag{21}$$

in which U_1, U_2 and U_3 are free parameters adjusted on the diffraction pattern measured at room temperature. Best estimates of the structure and experimental parameters were found thanks to the Chi-square minimization capabilities implemented in the nuclear data code CONRAD [36]. The angular offset (Eq. (20)) was determined at 300 K using a ThO_2 sample in a zircaloy-4 cladding measured on D1B under the same experimental conditions than the Zy4 rod sample [37]. Lattice parameters for thorium dioxide are rather well known at room temperature insuring a reliable determination of . Parameters of the response function of the spectrometers (Eq. (21)) were also determined at 300 K and kept fixed for all temperatures in order to avoid any mismatch with texture corrections. The latter corrections have been taken into account with the preferred orientation correction $P_{hkl}(\ _{hkl})$, involved in Eq. (4). They were determined iteratively with the lattice parameters as a function of temperature. These corrections, averaged over temperatures and reticular planes (hkl), are reported in Fig. 10. They are well reproduced by the von Mises distribution function proposed by Altomare et al. [38]:

$$P_{hkl}(\ _{hkl})\exp(p_0\cos(2\ _{hkl})), \tag{22}$$

in which p_0 is a free parameter. Results from D1B suggest that the Altomare's prescription provides a profile function in better agreement with our data compared to the more popular March–Dollase preferred orientation function [39, 40].

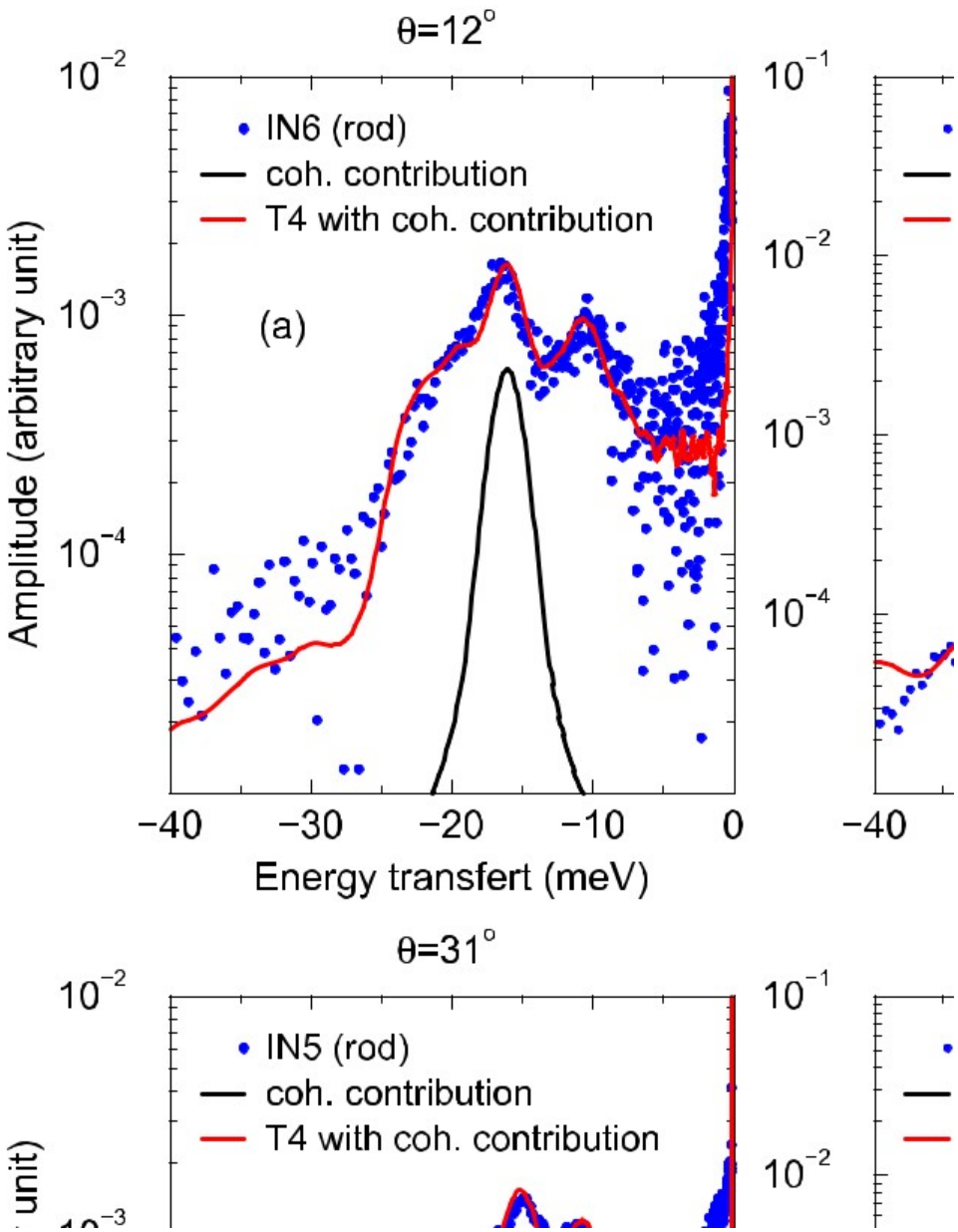

Fig. 7 Experimental symmetric dynamic structure factors compared to Tripoli- 4® simulations (T4) that encompass both coherent and incoherent terms in the inelastic neutron scattering cross section. The black dotted lines illustrate the contribution of the coherent part

Starting from the lattice parameters established by Goldak et al. [41] for pure α-Zr from 4.2 to 1130 K, our model converged towards the posterior solutions shown in Fig. 11. Figure 12 focuses on the qualitative description of the Bragg contributions corresponding to intermetallic precipitates $Zr(Fe,Cr)_2$ and zirconia ZrO_2. A reasonable agreement with the data was achieved thanks to a local adjustment of the various contributions and lattice parameters proposed in the Material Project database [17]. Around 70 meV, Bragg peaks measured with D20 are compatible with overlapping C14 and C15 Laves phase structures of $Zr(Fe,Cr)_2$, with a predominance of the cubic phase. A superposition of monoclinic (60%) and tetragonal (40%) phases can also reproduce the ZrO_2 structures observed at around 85 meV, with slightly different proportions than those quoted by Lelièvre et al. [6] (75% for monoclinic phase and 25% for tetragonal phase). These qualitative results aim confirming the importance of the stability of the tetragonal phase for modelling the growth of zirconia layers in zircaloy claddings [16, 42–44].

The lattice parameters *a* and *c* for the hexagonal close-packed crystal structure of α-Zr in Zy4 are reported in Fig. 13. Results deduced from the D1B and D20 diffraction patterns represent the first consistent set of experimental lattice parameters for low-hydrogenated zircaloy-4 sample established up to 700 K. The increase of the lattice parameters with the temperature was reproduced by the following expressions [45]:

$$a_{\mathrm{th}}(T) \; a_0 + a_0 \alpha_a \; \theta_D f_D \frac{\theta_D}{T} \quad , \tag{23}$$

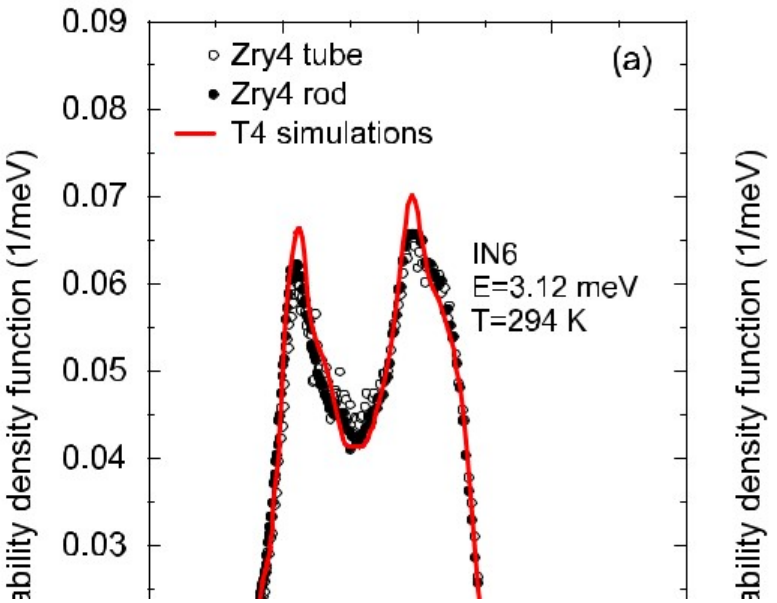

Fig. 8 Neutron-weighted multiphonon spectra measured at room temperature and simulated with Tripoli- 4®

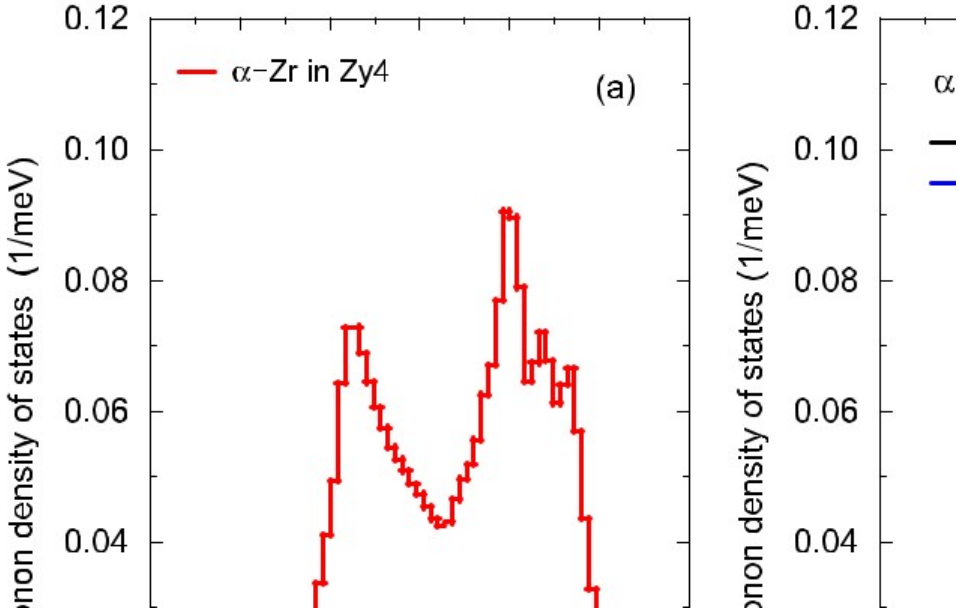

Fig. 9 The left-hand plot **a** represents the phonon density of states of α-Zr in Zy4 deduced from the IN5 and IN6 data. The right-hand plot **b** shows two ab initio results for pure α-Zr calculated by Blomqvist et al. [31] and Kagdada et al. [32] using the GGA and LDA approximations, respectively

$$c_{\mathrm{th}}(T) \quad c_0 + c_0 \alpha_c \, \theta_D f_D\!\left(\frac{\theta_D}{T}\right) , \tag{24}$$

in which a_0 (c_0) represents the lattice parameter at 0 K, α_a (α_c) stands for an average linear thermal expansion coefficient between 300 and 700 K, and θ_D is the Debye temperature. In the framework of the Debye model, the temperature dependence of the Debye integral f_D is given by:

$$f_D(x) \quad 3 \int_0^1 \frac{t^3}{\exp(t\,x) \quad 1} \mathrm{d}t . \tag{25}$$

The Debye temperature θ_D involved in this lattice parameter model was calculated from the phonon density of states ρ_X deduced from the IN5 and IN6 data (Fig. 9a). By introducing the harmonic-lattice heat capacity in a Debye model, the following compact expression [46]:

$$\theta_D \quad T \_ 35+5\sqrt{49+56\,\frac{1}{\kappa(T)} - 1} , \tag{26}$$

Table 3 Phonon density of states $\rho_X(\varepsilon)$ ($X \equiv$Zr) of α-Zr in zircaloy-4 (in 1/meV) as a function of the energy transfer ε (in meV) which correspond to the red line shown in Fig. 9a

ε	ρ Zr (ε)	ε	ρ Zr (ε)	ε	ρ Zr (ε)	ε	ρ Zr (ε)
0.8	0.0001	7.2	0.0145	13.6	0.0527	20.0	0.0896
1.2	0.0003	7.6	0.0175	14.0	0.0509	20.4	0.0789
1.6	0.0005	8.0	0.0205	14.4	0.0489	20.8	0.0646
2.0	0.0008	8.4	0.0235	14.8	0.0474	21.2	0.0674
2.4	0.0012	8.8	0.0284	15.2	0.0454	21.6	0.0721
2.8	0.0016	9.2	0.0337	15.6	0.0435	22.0	0.0678
3.2	0.0021	9.6	0.0411	16.0	0.0426	22.4	0.0612
3.6	0.0027	10.0	0.0493	16.4	0.0431	22.8	0.0641
4.0	0.0033	10.4	0.0644	16.8	0.0465	23.2	0.0666
4.4	0.0042	10.8	0.0728	17.2	0.0497	23.6	0.0569
4.8	0.0051	11.2	0.0729	17.6	0.0519	24.0	0.0436
5.2	0.0063	11.6	0.0689	18.0	0.0557	24.4	0.0328
5.6	0.0076	12.0	0.0644	18.4	0.0625	24.8	0.0173
6.0	0.0092	12.4	0.0607	18.8	0.0670	25.2	0.0108
6.4	0.0111	12.8	0.0574	19.2	0.0769	25.6	0.0082
6.8	0.0129	13.2	0.0545	19.6	0.0905	26.0	0.0050

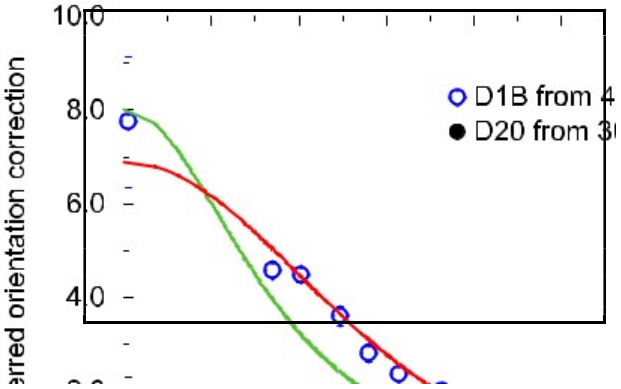

Fig. 10 Preferred orientation correction $P_{hkl}(\ _{hkl})$, averaged over temperatures and reticular planes (hkl), as a function of the orientation angle deduced from the diffraction patterns measured with D1B and D20. The solid red lines represent the von Mises distribution function proposed by Altomare et al. [38]. The dashed green lines represents the March–Dollase preferred orientation function [39, 40]

with

$$\kappa(T) = \int_0^{+\infty} \frac{2k_B T}{\omega} \sinh\left(\frac{\omega}{2k_B T}\right)^{-2} \rho_X(\omega)\mathrm{d}\omega, \tag{27}$$

provides a Debye temperature equal to θ_D 259(4) K. This value is in good agreement with ab initio results calculated for other zirconium alloys, such as ZIRLO^{TM} (θ_D =264.1 K) or M5^{TM} (θ_D =257.1 K) [47].

In Fig. 13, the solid red lines were obtained with a_0 3.2294 Å, c_0 5.1385 Å, α_a 5 × 10^{-6} K^{-1} and α_c 10 × 10^{-6} K^{-1}. At 298 K, the lattice parameters slightly increase up to a_{th} 3.2328 Å and c_{th} 5.1494 Å. Results reported in Table 4 illustrate the overall good agreement between the calculated lattice parameters and the experimental values extracted from the D1B and D20 diffraction patterns. The calculated lattice parameters are reported in Fig. 14. They are compared to temperature-dependent systematics retrieved from Ref. [48] and to experimental lattice parameters obtained for zirconium. The present work shows that lattice parameters for α-Zr in zircaloy-4 and for pure α-Zr are nearly equivalent in the case of low-hydrogenated zircaloy-4 samples.

5 Lattice parameter under neutron irradiation

In power nuclear reactors, zircaloy-4 claddings are exposed to severe neutron irradiation conditions whose effects, as a function of time, can be measured in terms of displacement per atoms (dpa), fluence (φ in n/m^2) or nuclear fuel burnup (BU in GWd/t). Strains in zirconium alloys come from many sources [49]. In this work, we limit ourselves to dimensional changes of the zircaloy-4 cladding, which depend on the hydrogen content and microstructures evolving with nuclear fuel burnup.

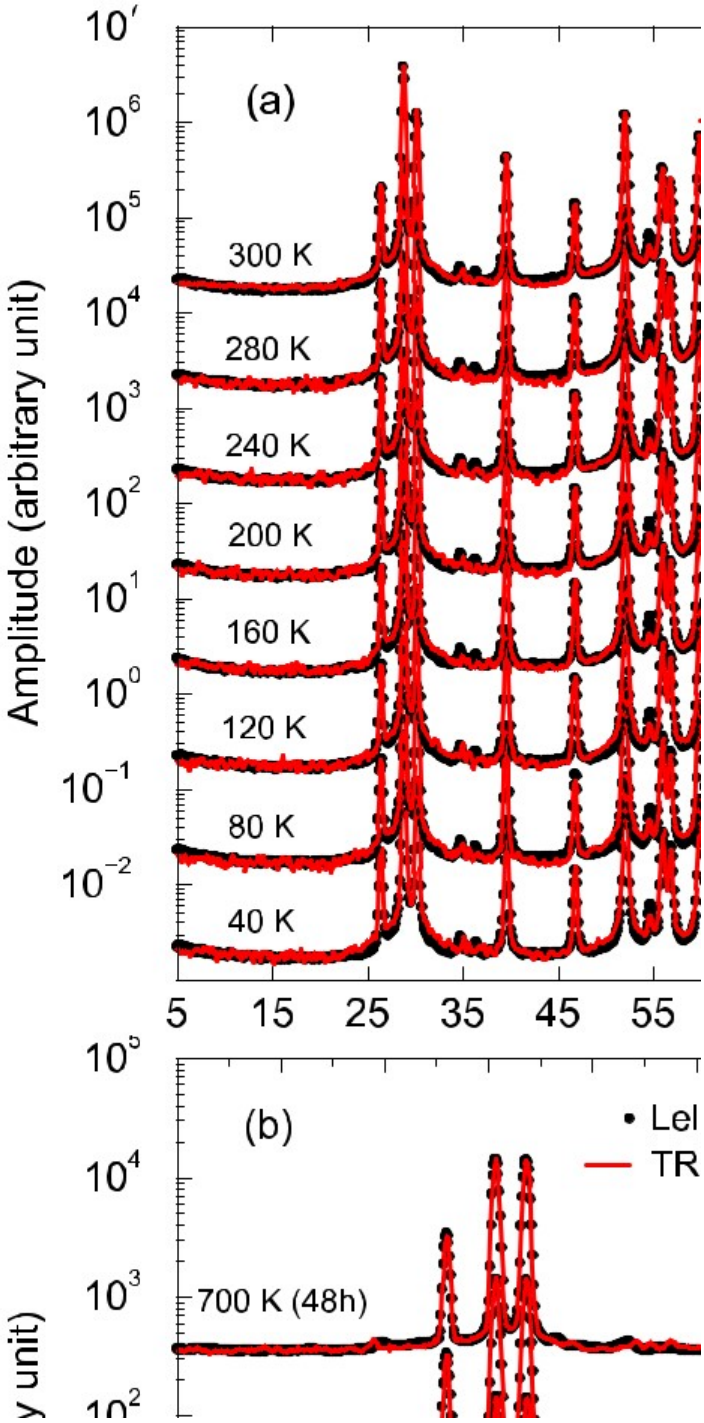

Fig. 11 Diffraction patterns measured with the D1B (1.28 Å) and D20 (2.42 Å) instruments. The laboratory scattering angle θ is equivalent to two times the angle θ_{hkl} between the incident neutron beam and the crystallographic reflecting plane

5.1 Hydrogenation correction

The impact of the hydrogen content x_H can be seen as a correction of the lattice parameters determined in the case of low-hydrogenated zircaloy-4 samples (Eqs. (23) and (24)):

$$a_{x_H}(T) \quad a_{\text{th}}(T) + \quad a(x_H), \tag{28}$$

$$c_{x_H}(T) \quad c_{\text{th}}(T) + \quad c(x_H). \tag{29}$$

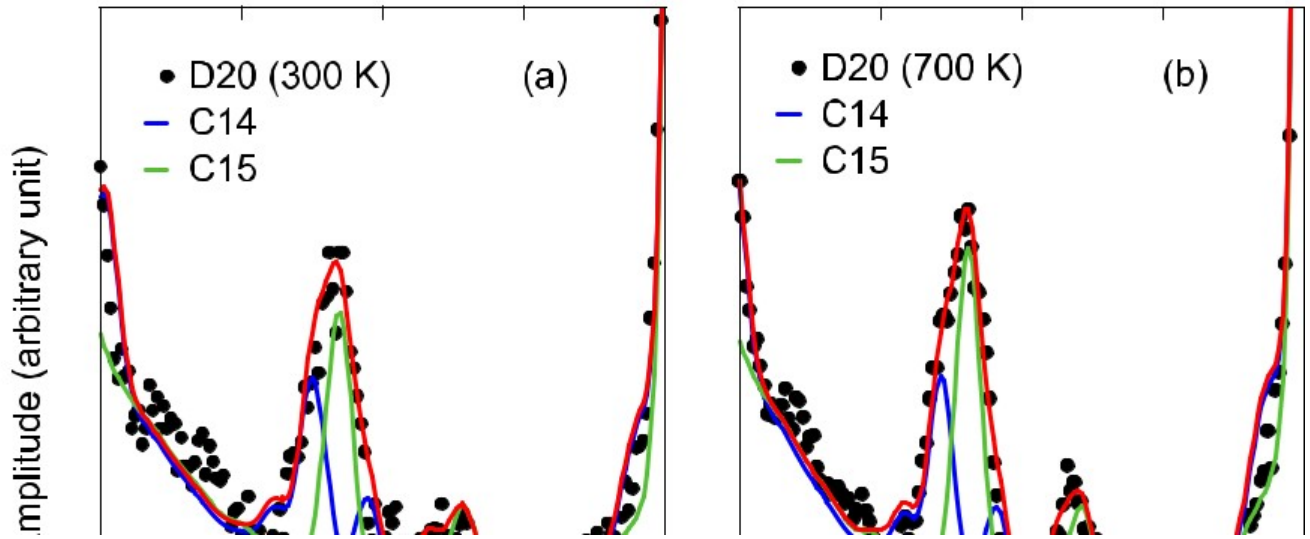

Fig. 12 Examples of Bragg peaks measured with D20 at 300 and 700 K corresponding to $Zr(Fe,Cr)_2$ (structures C14 and C15) and ZrO_2 (monoclinic and tetragonal phases). The red line represents the total contribution

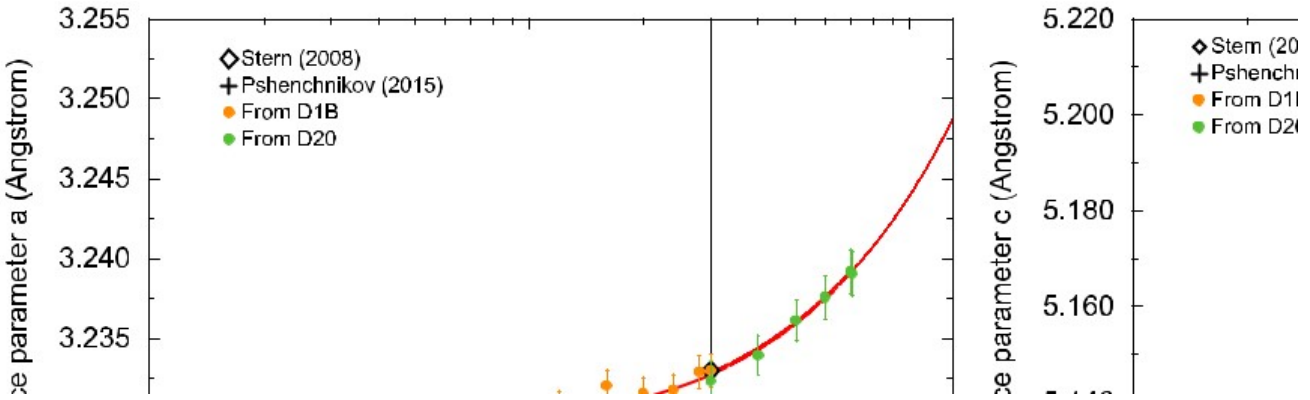

Fig. 13 Lattice parameters of α-Zr in Zy4 as a function of temperature for low-hydrogenated zircaloy-4 sample. The solid and dashed lines are obtained with Eqs. (23)–(27). The dot-dashed line indicates the room temperature. The experimental lattice parameters deduced from the D1B and D20 diffraction patterns are reported in Table 4

For the corrections $a(x_H)$ and $c(x_H)$, empirical expressions were established by Pshenichnikov et al. [50] for x_H ranging from 0 to 10,000 wppm:

$$a(x_H) \; 1.0 \times 10^{-7} x_H, \tag{30}$$

$$c(x_H) \; 2.0 \times 10^{-6} + 4.0 \times 10^{-10} x_H^2 - 5.0 \times 10^{-14} x_H^3. \tag{31}$$

It is worth to mention that hydrogen content above □650 wppm corresponds to excessive oxide thicknesses, which are not realistic for PWR operating with zircaloy-4 cladding. A hydrogen content greater than 1000 wppm corresponds to accident scenario studies. The hydrogen content depends on power history and axial position in the core. Figure 15 shows a considerable spread between calculated hydrogen content as a function of nuclear fuel burnup. If we consider the average value reported in Ref. [52], the relationship between the hydrogen content (in wppm) and the nuclear fuel burnup (in GWd/t) can be expressed as follows:

$$x_H 12.5 + 6.4\,\mathrm{BU} - 0.17\,\mathrm{BU}^2 + 0.0039\,\mathrm{BU}^3 \text{ for BU} < 50 \text{ GWd/t}. \tag{32}$$

The impact of the hydrogenation process on the lattice parameters a and c is illustrated in Fig. 16 with experimental values obtained from precharged samples containing 642 and 3300 wppm of hydrogen [54, 55]. The comparison with the lattice parameters calculated for x_H 3300 wppm (solid red lines) confirms the weak hydrogen dependence of the lattice parameter a and shows how Eq. (31) is able to predict the increase of the lattice parameter c reported by Hong [55] in the temperature range of interest for nuclear applications (T < 700 K).

Table 4 Lattice parameters a and c of α-Zr in Zy4 for low-hydrogenated zircaloy-4 sample deduced from the D1B (40–300 K) and D20 (300–700 K) diffraction patterns (see Fig. 13). The lattice parameters a_{th} and c_{th} were calculated with Eqs. (23) and (24). The latest line of the table corresponds to lattice parameters deduced from the diffraction pattern measured at 700 K for 48 h

T (K)	a (Å)	a_{th} (Å)	$a - a_{th}$ (Å)	c (Å)	c_{th} (Å)	$c - c_{th}$ (Å)
40	3.2289 (10)	3.2294	–0.0005	5.1395 (17)	5.1386	0.0009
80	3.2298 (10)	3.2297	0.0001	5.1404 (17)	5.1395	0.0009
120	3.2306 (10)	3.2301	0.0005	5.1408 (17)	5.1410	–0.0002
160	3.2320 (10)	3.2307	0.0013	5.1422 (17)	5.1428	–0.0006
200	3.2315 (10)	3.2313	0.0002	5.1439 (17)	5.1446	–0.0007
240	3.2317 (10)	3.2319	–0.0002	5.1459 (17)	5.1466	–0.0007
280	3.2329 (10)	3.2325	0.0004	5.1468 (17)	5.1485	–0.0017
300	3.2329 (10)	3.2328	0.0001	5.1484 (17)	5.1495	–0.0011
300	3.2323 (12)	3.2328	–0.0005	5.1488 (15)	5.1495	–0.0007
400	3.2339 (12)	3.2344	–0.0005	5.1547 (16)	5.1545	0.0002
500	3.2361 (13)	3.2360	0.0001	5.1601 (17)	5.1595	0.0006
600	3.2375 (13)	3.2376	–0.0001	5.1641 (18)	5.1646	–0.0005
700	3.2391 (14)	3.2392	–0.0001	5.1700 (19)	5.1697	0.0003
700	3.2390 (14)	3.2392	–0.0002	5.1708 (19)	5.1697	0.0011

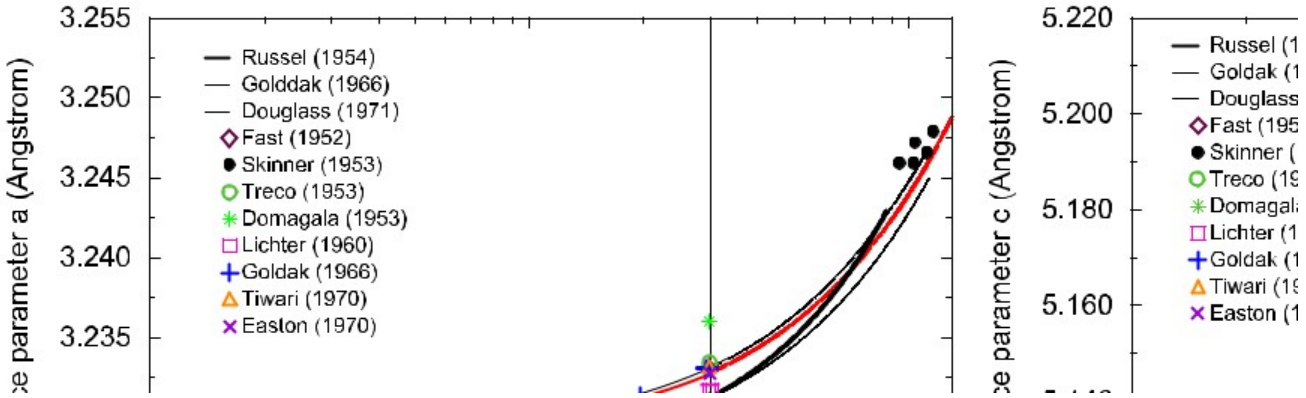

Fig. 14 α-Zr lattice parameters as a function of temperature compared to lattice parameters of α-Zr in Zy4 (solid red lines) as plotted in Fig. 13. The dot-dashed line indicates the room temperature

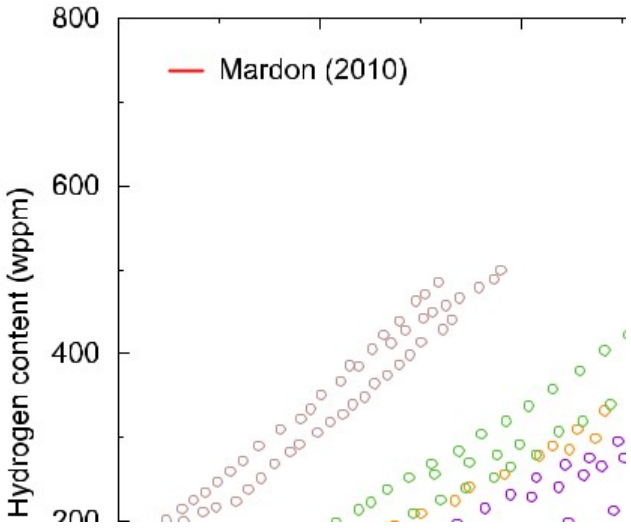

Fig. 15 Hydrogen content x H as a function of nuclear fuel burnup (BU) for PWR operating with zircaloy-4 cladding. Open circles represent a few results from Raynaud et al. [51] calculated for various axial core positions and typical PWR power histories. Results from Mardon et al. [52] correspond to an average value (Eq. (32)) taken from Ref. [53]

5.2 Neutron irradiation growth correction

The irradiation growth not only depends on hydrogen, but also on dislocation loops that form in zircaloy-4 under neutron irradiation. They can be classified into the prismatic loops (a-loop) and the basal loops (c-loop). Models based on a Cluster Dynamics

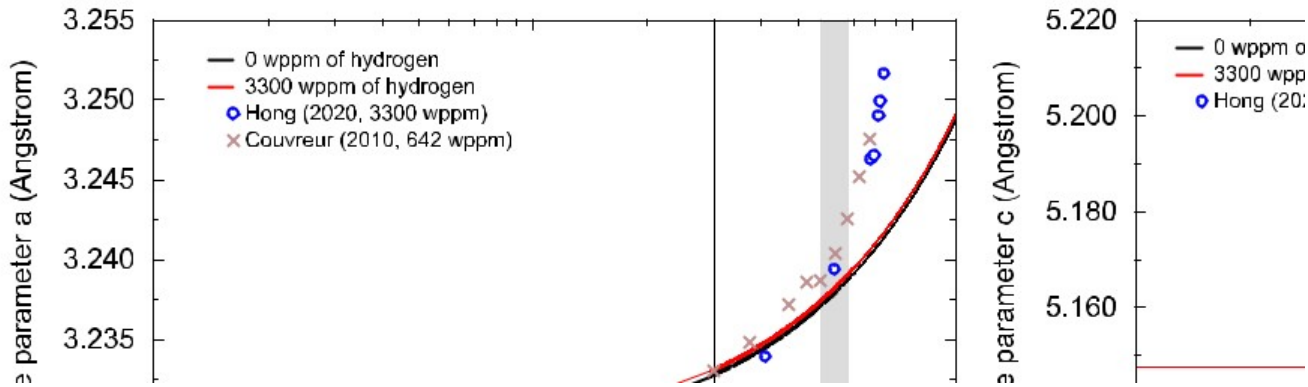

Fig. 16 Lattice parameters of α-Zr in zircaloy-4 as a function of temperature and hydrogen content. The thermal expansion reported by Couvreur et al. in Ref. [54] is normalized to D1B results at 300 K. The solid and dashed black lines is the lattice parameters of α-Zr in Zy4 for low-hydrogenated sample as plotted in Fig. 13. The solid and dashed red lines are obtained with Eqs. (28)–(31) for x H 3300 ppm. The dot-dashed line indicates the room temperature, and the grey zone locates the temperature range of interest for normal PWR operating conditions

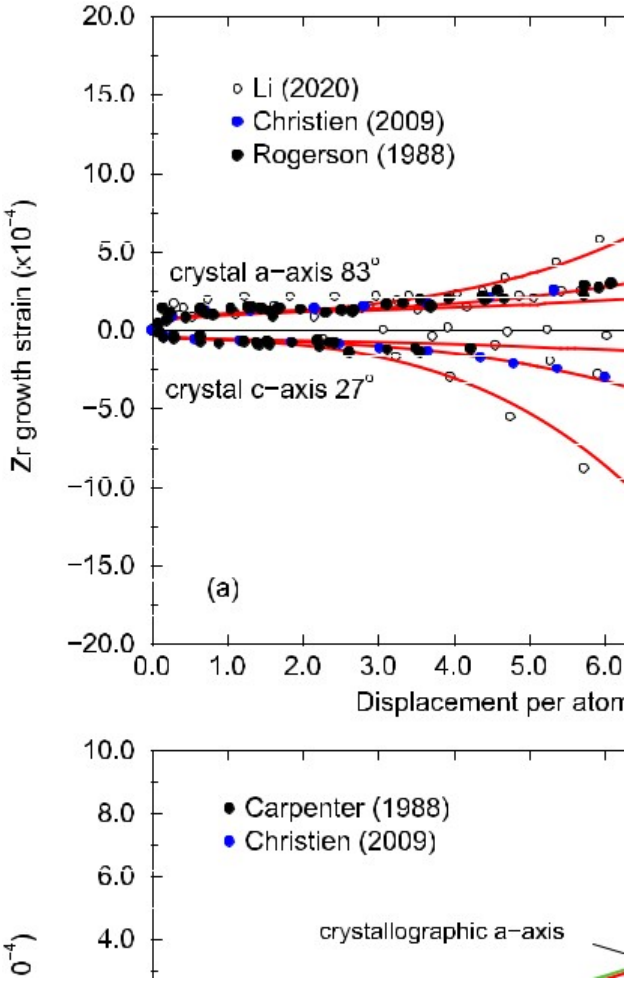

Fig. 17 Growth strains for single crystal of zirconium based on experimental [58] and theoretical [56, 57, 59] results. The top plot **a** shows results along the crystal axis. The bottom plot **b** shows results along the crystallographic axis. The solid red lines were obtained with expressions 35 and 36. The solid green lines take into account crystallographic orientation corrections δ_a 1.03 and δ_c 1.36 involved in Eqs. (33) and (34)

approach are mature to describe the evolution of the dislocation loop density as a function of irradiation time and temperature. These models were applied in Refs. [56, 57] to reproduce single crystal growth strains measured with annealed pure zirconium samples [58]. Experimental and theoretical results are reported in Fig. 17a for temperatures ranging from 523 to 583 K. The magnitude obtained for the growth strain along the crystal axis should be taken with care. As indicated in Ref. [57], temperature-dependent parameters involved in the irradiation growth of zirconium alloys are poorly documented in the literature and nucleation mechanisms at elevated temperature still required further theoretical refinements.

The competitive strains between hydrogen and microstructures on the average lattice parameters a and c can be summarized as follows:

$$a(T) \quad a_{x\,H}(T)(1+\delta_a\,\varepsilon_a(T)), \tag{33}$$

$$c(T) \quad c_{x\,H}(T)(1-\delta_c\,\varepsilon_c(T)), \tag{34}$$

in which $a_{x\,H}$ ($c_{x\,H}$) accounts for the hydrogen effects presented in Sect. 5.1 and ε_a (ε_c) represents the irradiation growth deduced from Zr single crystal strains corrected for crystallographic orientation δ_a (δ_c). The anisotropic strain observed for the a-axis and c-axis was calculated with the following expressions, whose parameters were adjusted using both experimental and theoretical works shown in Fig 17a:

$$\varepsilon_a(T) \quad \mathrm{dpa}^{1/5} + (1.2177 - 4.649\times10^{-3}\,T + 4.4444\times10^{-6}\,T^2)\,\mathrm{dpa}^3, \tag{35}$$

$$\varepsilon_c(T) \quad 0.6\,\mathrm{dpa}^{1/5} + (2.4479 - 9.384\times10^{-3}\,T + 9.0\times10^{-6}\,T^2)\,\mathrm{dpa}^3. \tag{36}$$

Figure 17b highlights the differences between strains along the crystallographic axes and strains along the main axis of the single crystal. These differences are due to crystallographic orientations of the a-axis and c-axis of the single crystal, which are close to 83° and 27° respectively. From the results reported in Refs. [56, 59], the crystallographic orientation corrections involved in Eqs. (33) and (34) were found to be close to δ_a 1.03 and δ_c 1.36.

Equations (33)–(36) represent a set of expressions that allow estimating the average lattice parameters of α-Zr in Zy4 under neutron irradiation. For presenting the results as a function of nuclear fuel burnup, we used a relationship between dpa and fluence that was deduced from the work of Carpenter et al. [59]:

$$\mathrm{dpa} \quad 0.1143\times10^{-24}\varphi, \tag{37}$$

and the relationship between fluence and nuclear fuel burnup proposed by Geelhood [60]:

$$\varphi 1.67\times10^{24}\,\mathrm{BU}\,. \tag{38}$$

Figure 18 summarizes the behaviour of the lattice parameters of α-Zr in Zy4 as a function of temperature and nuclear fuel burnup calculated with Eqs. (33)–(38). The first part of the curves represents the increase of the lattice parameters at zero nuclear fuel burnup up to 600 K. This temperature corresponds to hot full power condition in PWR. The second part of the curves corresponds to the behaviour of the average lattice parameters as a function of nuclear fuel burnup at constant temperature (T 600 K). The maximum burnup of 50 GWj/t represents an irradiation time of more than three-year fuel cycles.

The results as a function of nuclear fuel burnup confirm that the increase of the lattice parameters due to the hydrogenation process is rather negligible compared to the contribution of the dislocation loops. Indeed, between 0 and 50 GWj/t at T 600 K, the expansion along the a-axis is expected to be close to +0.008 Å and the contraction along the c-axis could reach −0.035 Å. The higher strain obtained for the c-axis is consistent with the nucleation mechanism of c-loop type vacancies that are favoured at elevated temperature due to higher diffusivity of mobile defects [57].

5.3 Discussions

Establishing usable relationships between the various studies on zircaloy-4 is a cumbersome task due to the extensive literature available on this nuclear material. In this work, a few of them were selected in view of calculating neutron induced scattering cross sections (Eqs. (4) and (6)) by including some experimental and theoretical material properties. Fine 3D Monte Carlo neutron transport simulations across the microstructure of zircaloy-4 under irradiation is not possible. Alternatively, material properties can be averaged over parameters involved in the neutron scattering theory. Irradiation growth of zircaloy-4 is well adapted to this empirical approach since it is approximately a constant volume process in the absence of external stress.

The starting point of our study was to confirm that the static and dynamic structure factor of α-Zr in zircaloy-4 and for pure α-Zr are nearly equivalent in the case of low-hydrogenated samples, ot equivalently non-irradiated samples. Such a statement was not so obvious because of the lack of the experimental results on zircaloy-4 available in the literature. This opens the safe possibility to consider some of the previous results obtained for pure zirconium, such as ab initio calculations and experiments carried out on single Zr crystal.

By collecting results for Zy4 and pure Zr, this study points out that irradiation growth of zircaloy-4 in PWR conditions can be treated as corrections of the lattice parameters established for non-irradiated samples. The complexity of the irradiation growth due to hydrogen diffusion or nucleation mechanisms of dislocation loops is well documented. Their effects as a function of temperature and irradiation time can thus be adequately summarized via Eqs. (33)–(38). The present study is then the first that provides an overview of the Zy4 structure parameters over a wide range of temperature and nuclear fuel burnup conditions over which the hexagonal phase exists. The obtained systematics will be made available to calculate the low-energy neutron scattering cross section of zircaloy-4 via Thermal Scattering Law files distributed along with the Evaluated Nuclear Data Library JEFF [61], hosted at the OECD/NEA databank.

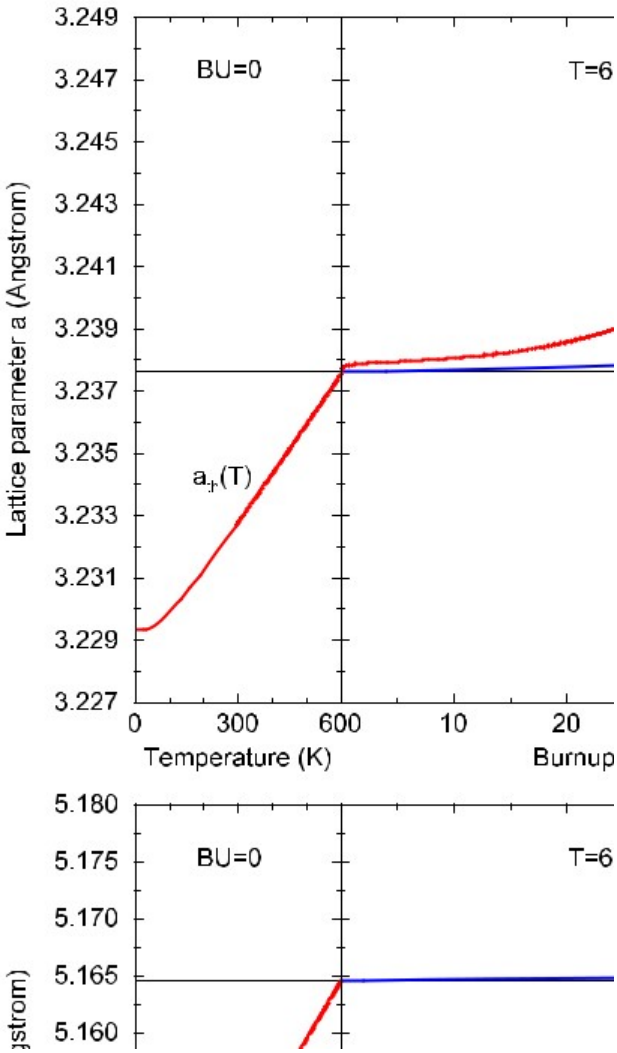

Fig. 18 The solid red line represents the lattice parameters for α-Zr in zircaloy-4 as a function of temperature and nuclear fuel burnup (BU) calculated with Eqs. (33)–(38). The solid blue line accounts for the hydrogen contribution only. The temperature T 600 K represents the average temperature of the zircaloy-4 cladding for normal PWR operating conditions

6 Conclusions

The ILL instruments offered the possibility to revisit the neutron scattering on low-hydrogenated zircaloy-4 samples over the temperature range of interest for PWR operating in normal conditions (T < 700 K). The IN6 and IN5 spectrometers provided the first experimental neutron-weighted multiphonon spectra of zircaloy-4 at room temperature, from which the coherent and incoherent inelastic parts of the phonon density of states were deduced thanks to Monte Carlo simulations. The resulting Debye temperature of θ_D 259 (4) K represents a valuable insight for further theoretical studies. The D1B and D20 diffractometers allowed exploring the structure of low-hydrogenated samples as a function of temperature, confirming that lattice parameters for α-Zr in zircaloy-4 and for pure α-Zr are nearly equivalent. The lattice parameters extrapolated at 0 K are close to a_0 3.2294 Å and c_0 5.1385 Å. At 298 K, they slightly increase up to a 3.2328 Å and c 5.1494 Å. The average linear thermal expansion coefficient between 300 and 700 K are α_a 5 × 10^{-6} K^{-1} along the a-axis and α_c 10 × 10^{-6} K^{-1} along the c-axis. By combining these results with irradiation growth corrections deduced from the literature, an empirical model was established to calculate the anisotropic variation of the average lattice parameters of α-Zr in zircaloy-4 under neutron irradiation as a function of nuclear fuel burnup in the temperature range over which this hexagonal phase exists.

A next step would consist to better link properties of the intermetallic precipitates and zirconia layer growth mechanisms. In this work, the contributions of iron, chromium and oxygen are only treated qualitatively through the observation of Bragg peaks corresponding to overlapping C14/C15 Laves phase structures of $Zr(Fe,Cr)_2$ and monoclinic/tetragonal phase structures of ZrO_2. Studies of these intermetallic precipitates and zirconia similar to the present one for αZr in zircaloy-4 would be needed. Available results reported in the literature seem sufficiently exhaustive for establishing further empirical laws valid for PWR conditions.

Acknowledgements The authors wish to express their appreciations for the experimental work performed at ILL. IN6 is operated by LLB as French CRG at ILL. Tripoli- 4® is a registered trademark of CEA. The authors would like to thank Electricite De France (EDF) for partial financial support.

Author contributions G. Noguere and S. Xu contributed to methodology, software, writing, review, and editing. A. Filhol and J. Ollivier contributed to sample preparation, experimental support, raw data analysis, review, and editing. J-M. Zanotti, G. Berrod, V. Nassif, I. Ouente Orench, C. Colin, T. Hansen, and D. Bernard were involved in experimental support and raw data analysis.

Funding This work is carried out in the framework of the SINET project funded by the CEA.

Data availability statement IN5: https://doi.ill.fr/10.5291/ILL-DATA.1-04-241; IN6: https://doi.ill.fr/10.5291/ILL-DATA.1-04-184; D1B: https://doi.ill.fr/ 10.5291/ILL-DATA.CRG-2771. This manuscript has associated data in a data repository [Authors' comment: Data will be made available on request.]

Declarations

Conflict of interest The authors declare that they have no conflict of interest to report.

References

1. L. Whitmarsh, Review Of Zircaloy-2 and Zircaloy-4 Properties Relevant to N.S. Savannah Reactor Design, ORNL-3281 Report, Oak Ridge National Laboratory (1962)
2. X. Iltis et al., J. Nucl. Mater. **224**, 121 (1995)
3. Y. Dali et al., J. Nucl. Mater. **426**, 148 (2012)
4. M. Tupin et al., Corros. Sci. **98**, 478 (2015)
5. M. Tupin et al., Corros. Sci. **116**, 1 (2017)
6. G. Lelièvre et al., J. Alloys Compd. **347**, 288 (2002)
7. E. Brun et al., Ann. Nucl. Energy **65**, 151 (2015)
8. S. Xu et al., EPJ Nucl. Sci. Technol. **8**, 8 (2022)
9. R.E. MacFarlane, A.C. Kahler, Nucl. Data Sheets **111**, 2739 (2010)
10. H. Schober, J. Neutron Res. **17**, 109 (2014)
11. X.X. Cai, T. Kittelmann, Comp. Phys. Comm. **246**, 106851 (2020)
12. H. Sitepu, March-type models for the description of texture in granular materials, PhD, Curtin University (1998)
13. N. Selmi, A. Sari, Adv. Mater. Phys. Chem. **3**, 168 (2013)
14. P.F. Becher et al., J. Am. Ceram. Soc. **76**, 657 (1993)
15. W. Qin et al., Acta Mater. **55**, 1695 (2007)
16. J. Liao et al., J. Nucl. Mater. **528**, 151846 (2020)
17. A. Jain et al., APL Mater. **1**, 011002 (2013)
18. L. Van Hove, Phys. Rev. **95**, 249 (1954)
19. A.W. Solbrig, Am. J. Phys. **29**, 257 (1961)
20. G.L. Squires, Proc. Roy. Soc. A **212**, 192 (1952)
21. A. Sjolander, Arkiv for Fysik **14**, 315 (1958)
22. O. Arnold et al., Nucl. Instr. Meth. A **764**, 156 (2014)
23. B.O. Mukhamedov et al., Intermetallics **109**, 189 (2019)
24. M. Sternik, K. Parlinski, J. Chem. Phys. **122**, 064707 (2005)
25. P.P. Bose et al., Pramana **71**, 1141 (2008)
26. S. Yu et al., Roy. Soc. Chem. Adv. **7**, 4697 (2007)
27. B. Saha et al., J. Appl. Phys. **107**, 033715 (2010)
28. G. Noguere et al., Phys. Rev. B **102**, 134312 (2020)
29. G. Noguere et al., J. Chem. Phys. **155**, 024502 (2021)
30. S. Xu et al., Nucl. Inst. Meth. A **1002**, 165251 (2021)
31. J. Blomqvist et al., in *Int. Conf. on Environmental Degradation of Materials in Nuclear Power Systems-Water Reactors*, Structure and Thermodynamical Properties of Zirconium Hydrides from First-Principle (Colorado Springs, 2011)
32. H.L. Kagdada et al., Adv. Mat. Res. **1141**, 204 (2016)
33. H.M. Rietveld, J. Appl. Cryst. **2**, 65 (1969)
34. L.B. McCusker et al., J. Appl. Crys. **32**, 36 (1999)
35. G. Caglioti et al., Nucl. Instrum. **3**, 223 (1958)
36. C. De Saint Jean et al., EPJ Nucl. Sci. Technol. **7**, 10 (2021)
37. G. Noguere et al., EPJ Web Conf. **122**, 17002 (2023)
38. A. Altomare et al., J. Appl. Crystallogr. **27**, 1045 (1994)
39. A. March, Z. Kristalloqr., **81**, 285 (1932)
40. W.A. Dollase, J. Appl. Cryst. **19**, 267 (1986)
41. J. Goldak et al., Phys. Rev. **144**, 478 (1966)
42. A.J.G. Maroto et al., J. Nucl. Mater. **229**, 79 (1996)
43. E. Polatidis et al., J. Nucl. Mater. **432**, 102 (2013)
44. K. Suchorab et al., Mater. Charact. **205**, 113373 (2023)
45. H. Kroncke et al., Acta Phys. Pol. **114**, 1193 (2008)
46. R. Passler, Adv. Condens Matter Phys., Article ID 9321439 (2017)
47. P.F. Weck et al., Dalton Trans. **44**, 18769 (2015)
48. R.A. Versaci, M. Ipohorski, *Temperature dependence of lattice parameters of alpha-zirconium*. (CNEA Report, Buenos Aires, 1991)
49. R.B. Adamson et al., J. Nucl. Mater. **521**, 167 (2019)
50. A. Pshenichnikov et al., Nucl. Eng. Des. **283**, 33 (2015)
51. P.A.C. Raynaud, A.S. Bielen, *Cladding hydrogen based regulations in the Unites States* (Water Reactor Fuel Performance Meeting, Chengdu, 2011)
52. J.P. Mardon et al., in *Proc. of LWR Fuel Performance meeting*, M5™ a breakthrough in Zr Alloy (TopFuel, Orlando 2010)

53. I. Turque, Effet de fortes teneurs en hydrogene sur les proprietes metallurgiques et mecaniques des gaines en alliage de zirconium apres incursion a haute temperature, PhD Thesis, PSL University, Paris (2016)
54. F. Couvreur et al., *In situ neutron scattering study of hydrogen-containing zircaloy-4 alloys* (LLB Scientific Report, CEA Saclay, 1997)
55. T. Le Hong et al., Acta Mater. **199**, 453 (2020)
56. F. Christien, A. Barbu, J. Nucl. Mater. **393**, 153 (2009)
57. Y. Li, N. Ghoniem, J. Nucl. Mater. **540**, 152312 (2020)
58. A. Rogerson, J. Nucl. Mater. **159**, 43 (1988)
59. G.J.C. Carpenter et al., J. Nucl. Mater. **159**, 86 (1988)
60. K.J. Geelhood, *Fuel performance consideration and data needs for burnup above 62 GWd/t, Report PNNL-29368* (Pacific Northwest National Laboratory, Richland, 2019)
61. A.J.M. Plompen et al., Eur. Phys. J. A **56**, 181 (2020)